Investigation of the local structure of molten ThF$_4$–LiF and ThF$_4$–LiF–BeF$_2$ mixtures by high-temperature X-ray absorption spectroscopy and molecular-dynamics simulation

Jian Sun,[a]‡ Xiaojing Guo,[b]‡ Jing Zhou,[a] Jianxing Dai,[a] Sanzhao Song,[a] Hongliang Bao,[a] Jian Lin,[a] Haisheng Yu,[a] Shangming He,[c] Feng Jiang,[a] Dewu Long,[a] Linjuan Zhang[a]* and Jian-Qiang Wang[a]*

[a]Key Laboratory of Interfacial Physics and Technology, Shanghai Institute of Applied Physics, Chinese Academy of Sciences, Shanghai 201800, People's Republic of China, [b]The Education Ministry Key Laboratory of Resource Chemistry and Shanghai Key Laboratory of Rare Earth Functional Materials, Department of Chemistry and Chemical Engineering, Shanghai Normal University, Shanghai 200234, People's Republic of China, and [c]Shanghai Synchrotron Radiation Facility, Shanghai 201204, People's Republic of China. *Correspondence e-mail: zhanglinjuan@sinap.ac.cn, wangjianqiang@sinap.ac.cn

The microscopic structures of ThF$_4$–LiF and ThF$_4$–LiF–BeF$_2$ molten salts have been systematically investigated by *in situ* high-temperature X-ray absorption fine-structure (XAFS) spectroscopy combined with molecular-dynamics (MD) simulations. The results reveal that the local structure of thorium ions was much more disordered in the molten state of the ThF$_4$–LiF–BeF$_2$ salt than that in ThF$_4$–LiF, implying that the Th and F ions were exchanged more frequently in the presence of Be ions. The structures of medium-range-ordered coordination shells (such as Th–F$_{2nd}$ and Th–Th) have been emphasized by experimental and theoretical XAFS analysis, and they play a significant role in transport properties. Using MD simulations, the bonding properties in the molten ThF$_4$–LiF and ThF$_4$–LiF–BeF$_2$ mixtures were evaluated, confirming the above conclusion. This research is, to the best of our knowledge, the first systematic study on the ThF$_4$–LiF–BeF$_2$ molten salt via quantitative *in situ* XAFS analysis and MD simulations.

1. Introduction

Molten-salt reactors (MSRs) (Abram & Ion, 2008; Kelly, 2014), as one of the six promising generation IV nuclear energy systems, have marked significant advantages of sustainability, economics, safety and proliferation resistance. The MSR system is the only liquid nuclear energy reactor using molten salt as a carrier and primary coolant. The choice of molten salt as a component is critical to the performance of MSRs and it must meet several requirements such as excellent neutron performance, lower melting point, appropriate viscosity and good tolerance for actinides or fission products. The cations and anions in the molten salts form a loose network in the form of ionic melts, molecular complexes or polymer clusters, depending on the temperature and concentration. These microscopic structures and dynamic behaviors are directly linked to the physico-chemical property of actinides or fission product elements in the molten salts (Olander *et al.*, 2012). Therefore, understanding the distribution, coordination and oxidation state of the different ionic species dissolved in these salts is necessary. In an MSR, different fuel salt compounds containing ThF$_4$ and UF$_4$ dissolved in NaF, LiF and LiF-BeF$_2$ have been proposed based on neutronic considerations (Delpech *et al.*, 2009; Mathieu *et al.*, 2006).

ThF$_4$-LiF-BeF$_2$ Molten Salt
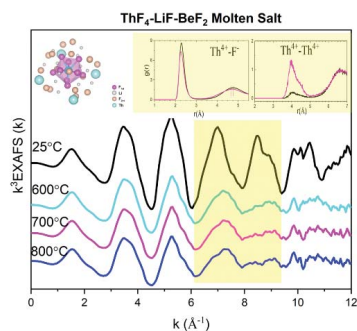
Owing to the radioactive risks, high-temperature corrosiveness and sensitivity to moisture and oxygen, experimental studies of molten fluoride systems are extremely challenging and have not been extensively reported.

To date, experimental studies of fluoride systems mainly focus on non-destructive spectroscopic methods, *e.g.* Raman spectroscopy, nuclear magnetic resonance (NMR) and X-ray absorption fine-structure (XAFS) spectroscopy. Toth and co-workers (Toth, 1971; Toth & Boyd, 1973; Toth *et al.*, 1973) have investigated the coordination structures of Th(IV), U(IV) and Zr(IV) in LiF-NaF molten salts using Raman spectroscopy. Eight coordinated Th(IV)/U(IV) systems were identified with excess fluoride ions, while seven coordinated Th(IV)/U(IV) systems were identified in fluoride-ion-deficient melts. For the coordination of Zr(IV), the ZrF_x^{4-x} coordination species (where $x = 8, 7, 6$ and possibly 5 or 4) were inferred. Although Raman spectroscopy can be used to obtain the coordination structure for strongly covalent interacted liquid systems, it is difficult to identify each contribution when more than two contributions of species overlap in the spectra. ^{19}F high-temperature NMR spectra have been used to investigate the coordination structures in the $LiF–LnF_3$ (Ln = Y, Lu, Ce) and $ThF_4–LiF$ systems (Bessada *et al.*, 2007; Rollet, Bessada, Auger *et al.*, 2004; Rollet, Bessada, Rakhmatoulline *et al.*, 2004; Rollet *et al.*, 2005). However, the structural information in NMR spectroscopy is obtained by referring to the chemical-shift values of known references, and some rare-earth nuclei are difficult to observe due to their paramagnetic behavior. XAFS is a direct element-specific technique providing information on the oxidation states and coordination environment of elements in various media. Its significant advantage is in obtaining concrete values of structural parameters of specific elements in the multicomponent mixtures, such as inter-ionic distances, coordination numbers (CNs) and structural disorder factors. Smith *et al.* (2019) tested the local structure in $ThF_4–LiF$ and $ThF_4–NaF$ molten salts using high-temperature *in situ* XAFS measurements, observing the contraction of the Th–F distance in the first coordination shell and a decrease of signal amplitude due to increased disorder and anharmonic effects in the molten state. Bessada and co-workers (Pauvert *et al.*, 2010) studied the structure of the molten $ZrF_4–LiF$ system, combining high-temperature NMR and extended X-ray absorption fine-structure (EXAFS) experiments, which supported the coexistence of three different Zr-based complexes, $[ZrF_6]^{2-}$, $[ZrF_7]^{3-}$ and $[ZrF_8]^{4-}$. Matsuura *et al.* studied the local structure in the molten $PbF_2–LiF$, $ThF_4–LiF–CaF_2$, $TbF_3–LiF–CaF_2$ and $LnF_3–MF$ systems (Matsuura *et al.*, 2009; Numakura *et al.*, 2010, 2011; Watanabe *et al.*, 2005, 2006).

The $LiF–BeF_2$ eutectic mixture was selected as a solvent salt in the thorium molten salt reactor (TMSR) in China (Xu, 2016; Xu *et al.*, 2014). The few existing reports regarding the $LiF–BeF_2$ eutectic mixture were mainly based on first-principles calculations. BeF_4^{2-}, $Be_2F_7^{3-}$ and higher polymer network structures in the $LiF–BeF_2$ mixtures were reported, and the Li^+ cations can move quite independently from the fluoroberyllate network, which is directly correlated to the viscosity of the liquid (Liu *et al.*, 2014; Salanne *et al.*, 2006,

2007). The structure and transport properties of the $ThF_4–LiF–BeF_2$ molten salt were studied exclusively by molecular-dynamics (MD) simulations (Dai *et al.*, 2015; Guo *et al.*, 2019; Wang *et al.*, 2017), while experimental research on the local structure of thorium ions in the $LiF–BeF_2$ molten salt remains sparse. Herein, applying a previously developed *in situ* high-temperature XAFS device (He *et al.*, 2012), we report for the first time, to the best of our knowledge, the thorium L_3-edge XAFS data for the $LiF–BeF_2$ molten salt at a eutectic composition in the temperature range 600–800°C. Thorium L_3-edge XAFS data in the $ThF_4–LiF$ mixture were also collected for comparison. Combined with theoretical XAFS and MD simulations, the influence of microscopic structure on transport properties was evaluated.

2. Experimental and theoretical investigation

LiF (AR, 99.99% purity) was supplied by Shanghai China Lithium Industrial Co. Ltd. Highly purified $LiF–BeF_2$ (67 mol% LiF and 33 mol% BeF_2) binary eutectic salt was supplied by the Shanghai Institute of Organic Chemistry (SIOC), Chinese Academy of Sciences (CAS) (Zong *et al.*, 2016). ThF_4 (99.99% purity) was supplied by the Changchun Institute of Applied Chemistry, CAS. To prepare the $ThF_4–LiF$ and $ThF_4–LiF–BeF_2$ molten salts, we mixed 20 wt% ThF_4 with the appropriate LiF or $LiF–BeF_2$ salts, which were transferred to a furnace and calcined at 700°C for 7 h. The prepared eutectic was slowly cooled to ambient temperature and then a uniform part of the mixture was chosen.

To prepare the sample for XAFS measurement, appropriate mixtures of boron nitride and metal fluorides were pressed into tablets. The proportion of each constituent was calculated by taking into account the absorption coefficient relative to the tablet thickness using the program *Demeter*. Tablets 8 mm in diameter were pressed under 5 T cm^{-2} to obtain a thickness of 1 mm. The above operations were carried out in a glove box to avoid exposure to oxygen and water. The apparatus scheme under working conditions is designed for the transmission mode displayed in Fig. S1 of the supporting information, and it mainly includes a sample-containment cell, heating device, water-cooling configuration and position-adjusting mechanism. The experimental setup was designed to accommodate the specific requirements of high-temperature XAFS measurements on radioactive molten-salt materials. The maximum temperature of the furnace is 1100°C (He *et al.*, 2012).

The crystalline phase of the $ThF_4–LiF–BeF_2$ sample was analyzed by X-ray diffraction on an X'Pert Pro MPD using Cu $K\alpha$ irradiation. Th ions mainly existing in the form of Li_3ThF_7 are shown in Fig. S2. XAFS data were collected at beamline 14W1 of the Shanghai Synchrotron Radiation Facility with a Si(111) double-crystal monochromator in transmission mode (Yu *et al.*, 2015). The electron-beam energy of the storage ring was 3.5 GeV and the maximum stored current was approximately 210 mA. All of the XAFS experiments were carried out in a custom-built *in situ* XAFS instrument. The thorium L_3-edge XAFS data were analyzed

using the program *Demeter* (Ravel & Newville, 2005). The theoretical phase and amplitude functions were calculated using *FEFF* 9.0 (Rehr *et al.*, 2010). For EXAFS data fitting, the Fourier-transform window for *k* space was of the sine type in the range 2.8–11.3 Å and sine type for *R* space in the range 1–3 Å. The amplitude reduction factor S_0^2 was set to 0.9 (Zhang *et al.*, 2018). The double-electron excitations affect the EXAFS signal and can influence the result of the data analysis (Hennig, 2007; Gomilšek *et al.*, 2003; Benfield *et al.*, 1994; Kodre *et al.*, 2002). Thus, in thorium L_3-edge EXAFS experimental spectra, the double-electron excitations were subtracted as a reflection of the data translated to the position in energy of the excitation using the standard procedures in *Demeter*. Fig. S3 shows the uranium L_3-edge EXAFS data before and after subtracting the double-electron excitation in *k* and *R* space, in which the features at very low distances clearly improved. In fact, the CNs are expected to be influenced, whereas the influence on bond length from the double-electron excitations is minimal.

The MD simulations were performed for the ThF_4–LiF and ThF_4–LiF–BeF_2 molten salts at 600°C, 700°C and 800°C using the *FIST* module of the *CP2K* software package (Hutter *et al.*, 2014). In each simulation, particles were placed in a cubic box with periodic boundary conditions. Simulated annealing techniques were used to equilibrate the systems. Each system was first equilibrated in the isothermal–isobaric ensemble with a pressure of 0 Pa for 500 ps. The integral step used in the MD simulations was 1.0 fs. Then canonical NVT runs at the equilibrated cell volume were carried out for 2.0 ns with an integral step of 1.0 fs. Long-range electrostatic interactions were calculated using the Ewald method with periodic boundary conditions in all three dimensions (Essmann *et al.*, 1995). The short-range van der Waals interactions were computed with a cutoff of 1.1 nm. The Nosé method was used for the temperature and pressure couplings in all runs (Nosé, 1984). The polarizable ion model, which is described as the sum of four different contributions (charge–charge, dispersion, overlap repulsion and polarization), was used for the interaction between particles. The parameters are the same as those listed in our previous studies (Dai *et al.*, 2015; Guo *et al.*, 2019). The Th^{4+} polarizability was set to 7.6960 Bohr^3, and the F^- polarizability was set to 7.8935 Bohr^3.

3. Results and discussion

3.1. EXAFS analysis on ThF_4–LiF and ThF_4–LiF–BeF_2 compounds

The thorium L_3-edge X-ray absorption spectra were collected in the solid state (at room temperature) and the molten states (at 600°C, 700°C and 800°C) for ThF_4–LiF–BeF_2, as well as for ThF_4–LiF compounds. Fig. 1 shows the Fourier transform of EXAFS spectra in the ThF_4–LiF and ThF_4–LiF–BeF_2 compounds without phase-shift correction. According to the path analysis in *R* space, the peak at $R + \Delta$ values of approximately 1.9 Å, 4.0 Å and 4.5 Å correspond to the single-scattering path of nearest-neighbor fluorine atoms,
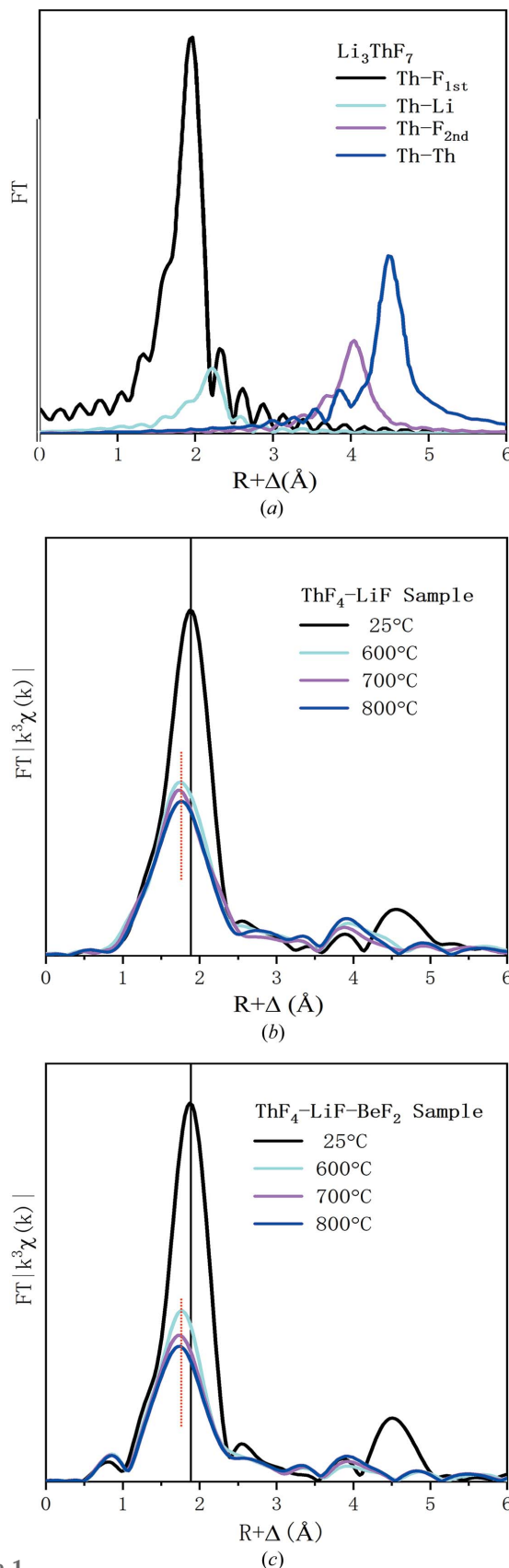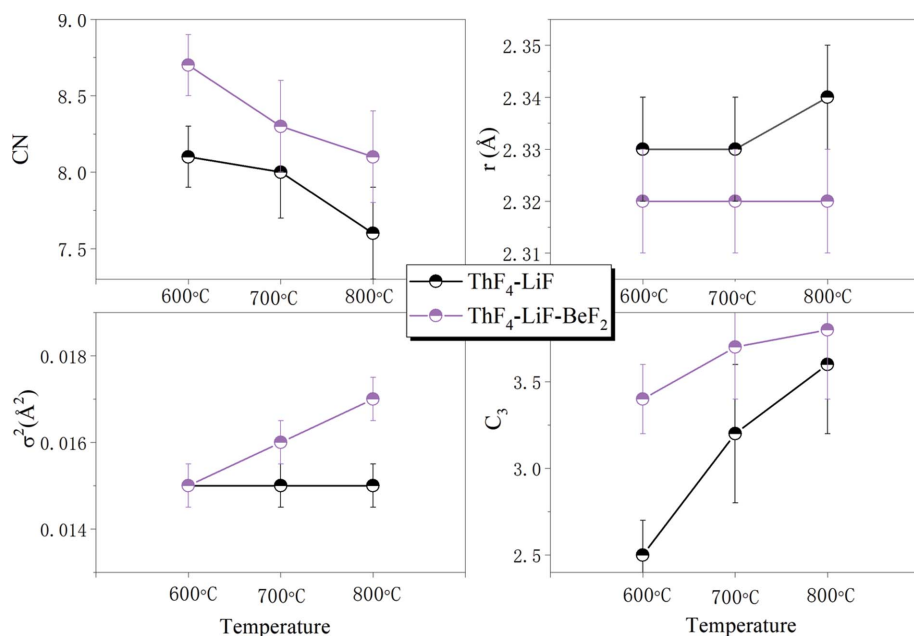

Figure 1
(*a*) Theoretical contributions of each individual path in Fourier transforms in standard Li_3ThF_7. Fourier transforms of experimental EXAFS spectra of (*b*) ThF_4-LiF and (*c*) ThF_4-LiF-BeF_2 molten salts versus temperature.

second solvation fluorine atoms and higher-distance thorium atoms, respectively. At first glance, compared with the solid phase in the ThF_4–LiF sample, we note that the amplitude of the first peak of the molten phase clearly decreases and shifts towards smaller distances, which is consistent with the results in previous studies (Bessada *et al.*, 2007; Smith *et al.*, 2019). This reduction and broadening of the peak are typical of an asymmetric pair distribution function characteristic of highly disordered systems. It is worth mentioning that the amplitudes of $Th-F_{2nd}$ in the second coordination shell of the molten phase are still noticeable in the ThF_4–LiF mixture, but previous investigations did not discuss this (Bessada *et al.*, 2007; Smith *et al.*, 2019). However, the disappearance of a higher-distance peak (∼4.5 Å) can be observed due to the absence of long-distance order in the molten phase. In the present work, *in situ* XAFS measurements at the thorium L_3-edge in the ThF_4–LiF–BeF_2 compounds were obtained at high temperature. The trace of structural changes in the ThF_4–LiF–BeF_2 compounds is consistent with that of the ThF_4–LiF mixture.

The quantitative local structural information can be extracted by curve fitting in R space, as shown in Table S1 of the supporting information and Fig. 2. In the solid phase, the CN of $Th-F_{1st}$ obtained in ThF_4–LiF is approximately 9.0 and the bond length is approximately 2.36 ± 0.01 Å, which are consistent with previous EXAFS results (Numakura *et al.*, 2011) and crystal-structure data (Laligant *et al.*, 1989) of Li_3ThF_7. With the addition of BeF_2, the bond length is slightly smaller than that in LiF molten salt, but the CN reaches 10 in the solid state, suggesting the rearrangement of Th and F ions in the LiF–BeF_2 binary salt. In the molten phase, an anharmonic vibration effect became prominent (Ferlat *et al.*, 2005, 2006; Filipponi, 2001), so the C_3 cumulant was introduced for

EXAFS fitting at high temperature (Bunker, 1983). The variation of CN, R, σ^2 and the C_3 cumulant at high temperature in ThF_4–LiF and ThF_4–LiF–BeF_2 compounds are shown in Fig. 2. In fact, relatively large errors are always expected when determining the CN, which ranges from 10% to 25% in the EXAFS fits (Ikeda-Ohno *et al.*, 2008; Sandström *et al.*, 2001; Hennig, 2007). Thus the change of CN is unauthentic. With increasing temperature, σ^2 and the C_3 cumulant increase gradually in both ThF_4–LiF and ThF_4–LiF–BeF_2 compounds. The Debye–Waller factor corresponds to the distribution of CN and the C_3 cumulant corresponds to the symmetry of the local structure. Therefore, both values are an indication of local structural disorder around Th^{4+}. In particular, the C_3 cumulant corresponds to the exchange degree of F coordinated around Th^{4+}. When the local structure around a focused cation is asymmetric and anions coordinated around a cation are exchanged frequently, these fluctuation factors indicate large values. Compared with those of ThF_4–LiF, σ^2 and the C_3 cumulant were relatively larger in the ThF_4–LiF–BeF_2 molten salt, indicating that Th and F ions were exchanged more frequently and the local structure of Th cations was much more disordered. Considering the limit of the maximum number of floating parameters by $2\Delta k \Delta R / \pi$ and possible obstruction of the signal-to-noise ratio induced by high-temperature thermal disorder, the current EXAFS fitting is insufficient to give further proof of the higher-coordination-distance effect in the ThF_4–LiF and ThF_4–LiF–BeF_2 molten phases.
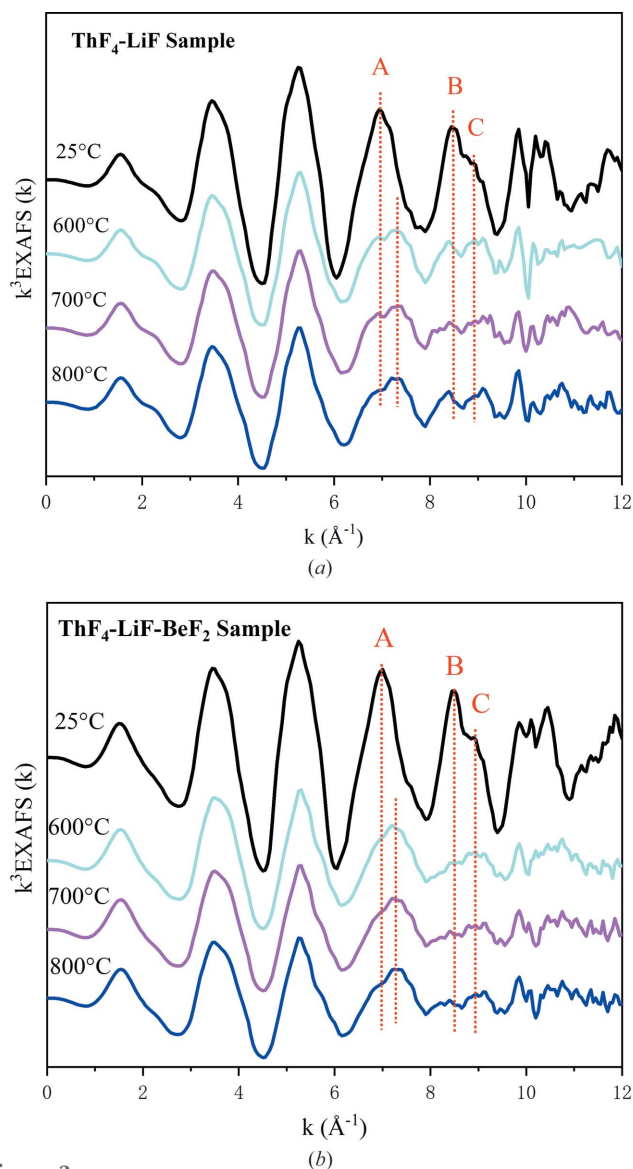
Fig. 3 shows thorium k^3-weighted EXAFS oscillations of ThF_4–LiF and ThF_4–LiF–BeF_2 compounds at different temperatures. The EXAFS oscillation is well known to be the superimposition of individual scattering paths from ligand s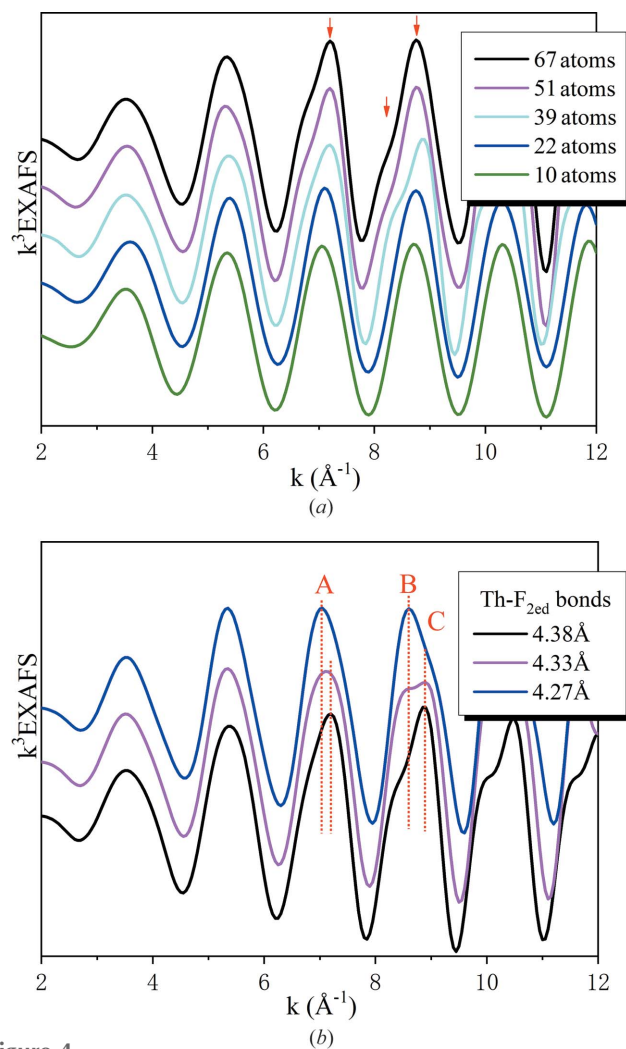hell atoms; therefore, pattern changes in EXAFS oscillations directly reflect the arrangement of local coordination atoms in the molten-salt phase. First, the main EXAFS oscillations of the Th L_3-edge are in rough agreement in k space, implying that the main structures are unchanged with temperature and salt configuration. Second, contrary to the case of the solid phase, overall damping of the oscillations occurs at high temperature, which is induced by the thermal disorder effect. Third, distinct EXAFS oscillation characteristics within the k range of 6–10 Å^{-1} induced by the temperature effect can be seen in both ThF_4–LiF and ThF_4–LiF–BeF_2 compounds. As marked by the dotted lines in Fig. 3, we can observe the shift of peak A and the weight change of the B/C ratio at high temperature. For example, at 600°C, the separated character of B and C in the ThF_4–LiF compound is more obvious than that in the ThF_4–LiF–BeF_2 compound. Such changes may indicate a

Figure 2
Variation of structural parameters of the molten ThF_4–LiF and ThF_4–LiF–BeF_2 mixtures, in which CN, R, σ^2 and the C_3 cumulant correspond to the coordination number, average interatomic distance, Debye–Waller factors and anharmonic oscillations at high temperature, respectively.

Figure 3
Weighted EXAFS oscillations as extracted from the Th L_3-edge absorption spectra of (*a*) ThF$_4$–LiF and (*b*) ThF$_4$–LiF–BeF$_2$ molten salts versus temperature.

Figure 4
(*a*) Comparison of multiple-scattering calculations for different atomic clusters of the Th L_3-edge for Li$_3$ThF$_7$. In the simulation, no thermal disorder effects were considered. (*b*) Comparison of EXAFS simulations in the Th L_3-edge with decreasing bond length between the thorium central atom and second solvation fluoride shell.

new coordination environment at high temperature that is different from the solid phase associated with increasing temperature and molten-salt configurations.

To understand the origin of fine character changes in the k^3-weighted EXAFS functions, we carried out EXAFS simulations using different atomic clusters around the thorium absorber based on the Li$_3$ThF$_7$ structural model shown in Fig. 4(*a*). For a cluster with thorium as the central atom, the first shell consists of nine F atoms, reproducing the main oscillation pattern effectively. For the 22-atom model, an additional 12 Li atoms were considered and no structural changes can be seen due to the weak scattering ability of Li atoms. With the number of atomic clusters reaching 39 atoms, 17 F atoms were added as the second solvation shell, and the most obvious cleavage occurs mainly at 6–10 Å^{-1} (marked by arrows). Upon continual increase of the size of the cluster, the
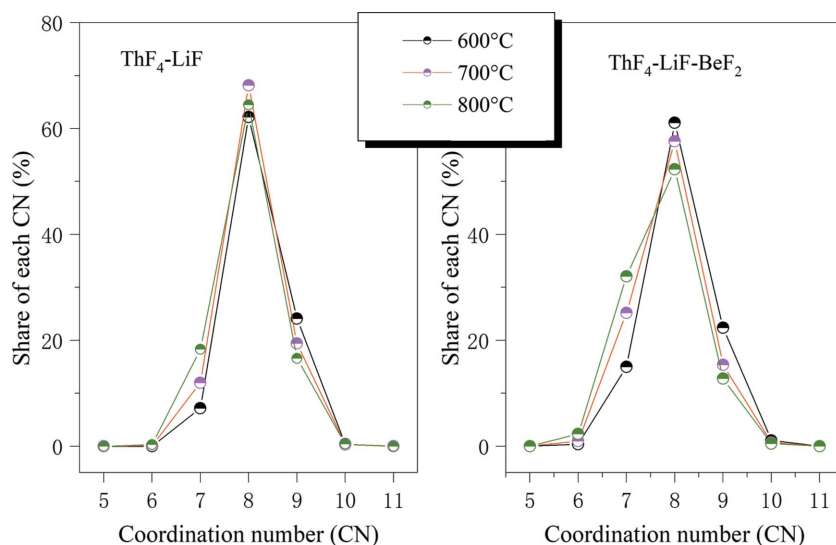
characters are passivated due to the superimposition contributions of the higher coordination shell and are finally stabilized. Based on the above discussion, we point out here the important role of the second F shell atoms that contributes to the separated peaks. To further track its impact, we simulated the EXAFS pattern variety induced by changing the Th—F$_{2nd}$ bond length as shown in Fig. 4(*b*). With decreasing Th—F$_{2nd}$ bond length, the position of peak A shifted and the weight of B/C changed, which is much closer to the experimental spectra of solid compounds (Fig. 3). In the molten phase, although the amplitude of experimental oscillation patterns decreases dramatically due to the thermal disorder effect, the character changes at 6–10 Å^{-1} are still prominent. Compared with the solid phase, at high temperature peak A shifts to a higher k value and the amplitude of peak B decreases, corresponding to the changing trend with elongated Th—F$_{2nd}$ bonds. Relative to the ThF$_4$–LiF compound, the weaker cleavage characters at 600°C are manifested because they superimpose more scat-

tering contributions from higher shells in the ThF_4–LiF–BeF_2 compounds, such as Th–Th. When the temperature reaches 800°C, the separated character of B and C are much clearer both in ThF_4–LiF and ThF_4–LiF–BeF_2 mixtures (shown in Fig. 3), originating from the further destruction of the medium-range-ordered structure.

3.2. Comparison with MD simulations

To clarify the effects of adding BeF_2 at different temperatures, MD simulations of ThF_4–LiF and ThF_4–LiF–BeF_2 mixtures were performed. The distributions of CN in different molten salts, as well as the influence of temperature T, are shown in Fig. 5. The CN was estimated according to the first minimum in a radial distribution function (RDF). An F^- is accepted in the first solvation shell of Th^{4+} if the distance between them is shorter than the distance corresponding to the first minimum of the RDF. Three dominant complexes are found to coexist in the melt: $[ThF_7]^{3-}$, $[ThF_8]^{4-}$ and $[ThF_9]^{5-}$, with the eightfold coordinated $[ThF_8]^{4-}$ complex always being the pre-dominant one. As expected, for both samples, the amount of lower-CN increases, while the amount of higher-CN decreases with temperature, resulting in a slight decrease of the average CN with increasing temperature. As presented by Numakura et al. (2011), the width of the CN distribution corresponds to the fluctuation factors (σ^2 and C_3 cumulant) in the EXAFS analysis. The dispersion tendency in ThF_4–LiF–BeF_2 mixtures can be observed with a more asymmetrical spectral pattern, which is consistent with EXAFS results. The variation difference of CN between ThF_4–LiF and ThF_4–LiF–BeF_2 mixtures may be related to the change of cation–anion bond length, local structural distortion and the Coulomb interaction induced by the addition of BeF_2. Therefore, it is necessary to evaluate bonding strength in the ThF_4–LiF and ThF_4–LiF–BeF_2 mixtures.

In pure LiF, the cation is fourfold coordinated, which is similar to that in the LiF–BeF_2 eutectic salt. Due to the lower charge, however, we would anticipate that the coordination of Li^+ with F^- is weaker than that of Be^{2+}, so the LiF–BeF_2 mixtures should first meet the coordination requirements of the Be^{2+} ion. The radial distributions shown in Fig. 6 are consistent with this. Indeed, the first RDF peak for the Be^{2+}–F^- pair is very sharp, with a high maximum and a very low minimum (nearly 0). In contrast, the first peak for Li^+—F^- is broader, and the first minimum is less pronounced, indicative of a more flex-

ible ion cluster that allows exchange of the F^- counter ions more frequently. When considering the ThF_4 effect in the molten salts, several obvious variations can be seen in the ThF_4–LiF and ThF_4–LiF–BeF_2 mixtures. First, the first peak produced by Th—F is near 2.3 Å, hardly varying with the existence of BeF_2. The position of the Th—F bond is consistent with previous reports (Dai et al., 2015; Dewan et al., 2013; Liu et al., 2014). Concerning the shape of the RDF, the first sharp peak of Th—F and the following deep minimum indicate the existence of comparatively stable clusters with a well defined first solvation shell. The height of the maximum of the first Th—F peak is approximately 8.5 in ThF_4–LiF mixtures and 7.5 in ThF_4–LiF–BeF_2 mixtures. In the ThF_4–LiF mixture, the Th^{4+}–F^- peak is much sharper, indicating that the local structure is much more stable. Second, the bond length of Th–F_{2nd} became shorter in the ThF_4–LiF–BeF_2 mixture. At the same time, the position of the first F—F peak also moved closer when BeF_2 was added to the molten salt. These results indicate that the $[ThF_x]^{4-x}$ network is compacted in ThF_4–LiF–BeF_2 mixtures, consistent with the result of the EXAFS

Figure 5
Percentage variations of CN at 600°C, 700°C and 800°C in ThF_4–LiF and ThF_4–LiF–BeF_2 mixtures.
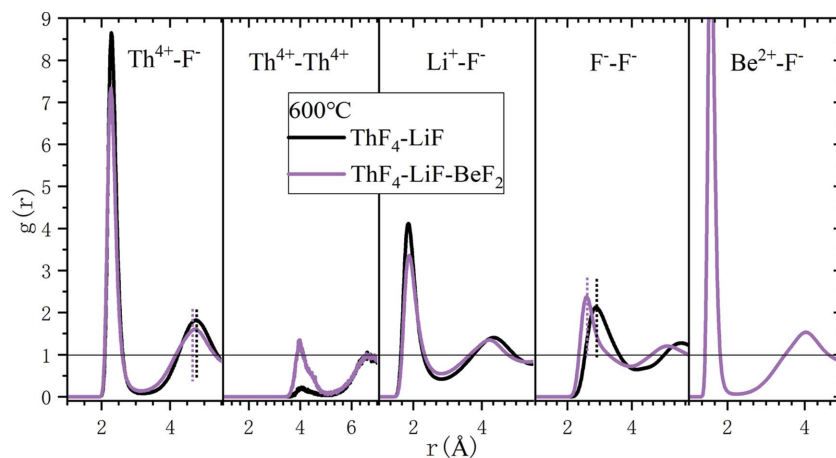
Figure 6
Radial distribution functions, $g(r)$, at 600°C in ThF_4–LiF and ThF_4–LiF–BeF_2 mixtures.

Table 1
Cage-out times (ps) of the Th^{4+} first solvation shells in ThF$_4$–LiF and ThF$_4$–LiF–BeF$_2$ mixtures at several temperatures.

	600°C	700°C	800°C
LiF–ThF$_4$	2.8	2.0	1.5
LiF–BeF$_2$–ThF$_4$	2.5	1.8	1.2

analysis. Third, a pronounced Th^{4+}–Th^{4+} peak appears at 4.0 Å in the ThF$_4$–LiF–BeF$_2$ molten-salt sample, which is smaller than twice the Th^{4+}—F$^-$ bond distance (∼2.3 Å), indicating a significant number of pairs of thorium cations bonded by nonlinear bridging fluoride anions. This provides further proof of the existence of Th–Th at the higher distance, supporting the spectral passivation observed in the EXAFS oscillation pattern of ThF$_4$–LiF–BeF$_2$ mixtures. Such a medium-range structural feature (Th–F$_{2nd}$ and Th–Th) was verified in the molten fluorides by MD simulations and may have an important impact on the transport properties.

To further investigate the bonding stability between Th and F ions in ThF$_4$–LiF and ThF$_4$–LiF–BeF$_2$ mixtures, the rate of the instantaneous CN change was evaluated by a cage-correlation-function analysis proposed by Salanne and co-workers (Pauvert *et al.*, 2011). A longer cage-out time indicates a more stable cluster. The usual way to define this lifetime (Glover & Madden, 2004) is the time for which the cage correlation function takes the value of $1/e$. The corresponding lifetimes have been extracted and are shown as a function of temperature in Table 1 and Fig. S6. With increasing temperature, the corresponding τ becomes smaller. The lifetimes of the Th^{4+} first solvation shell in ThF$_4$–LiF and ThF$_4$–LiF–BeF$_2$ mixtures at 600°C are 2.8 ps and 2.5 ps, respectively. Therefore, the stability of the Th–F cluster follows the order ThF$_4$–LiF > ThF$_4$–LiF–BeF$_2$. This result is consistent with the EXAFS results, implying that the Th and F ions were exchanged more frequently and the local structure of Th cations was much more disordered in the ThF$_4$–LiF–BeF$_2$ molten salt.

The stability of the first coordination shell can also be estimated by the potential of the mean force, defined as

$$V(r) = -k_B T\,[\ln g(r) + 2\ln(r)].$$

The effective potentials are characterized by a deep first minimum and a following peak in both molten salts as shown in Fig. 7. The energy barriers correspond to the energy difference between the first deep minimum and the following local maximum. The energy barrier for the Th^{4+}–F$^-$ dissociations in ThF$_4$–LiF and ThF$_4$–LiF–BeF$_2$ mixtures are 4.07($k_B T$) and 3.36($k_B T$), respectively, which is consistent with the calculated lifetimes. In agreement with the cage-out time, the energy barriers also decrease with temperature.

3.3. Viscosity

Shear viscosity is the resistance of a fluid to being deformed by shear forces and governs macroscopic transport properties. According to the Kubo–Green formula, viscosity can be
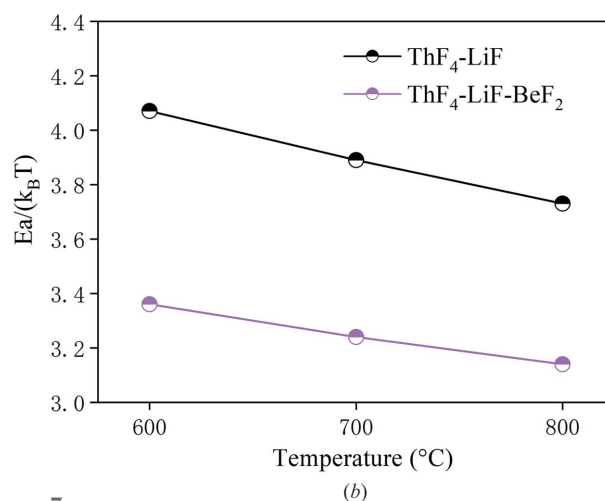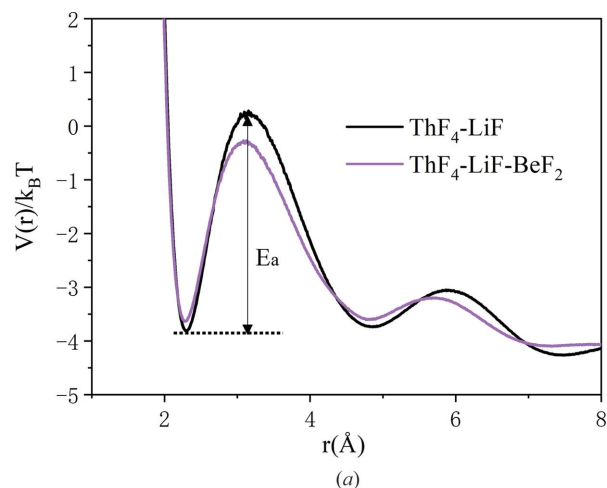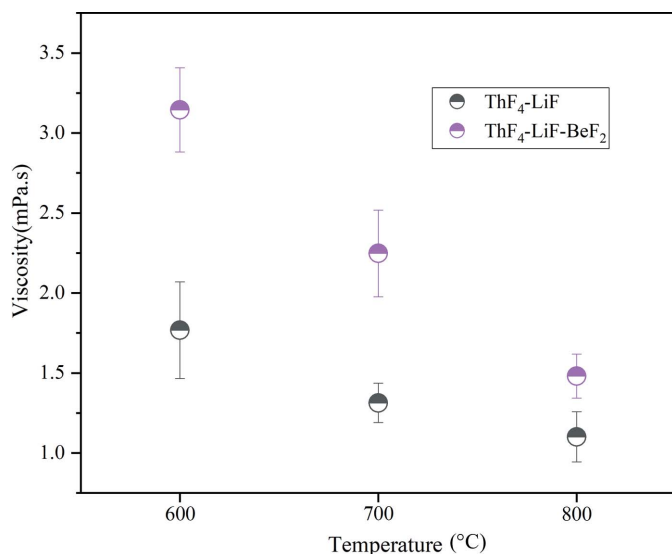
Figure 7
(*a*) Potentials of mean force for Th^{4+}–F$^-$ dissociation in ThF$_4$–LiF and ThF$_4$–LiF–BeF$_2$ mixtures at 600°C. (*b*) Activation energies (E_a) extracted from the potential of mean forces in ThF$_4$–LiF and ThF$_4$–LiF–BeF$_2$ mixtures at several temperatures.

calculated using the equilibrium MD method from the time integral of the shear stress autocorrelation requiring long runs to obtain good statistics,

$$\eta = \frac{1}{k_B T V}\int_0^\infty \langle\sigma_{xy}(t)\sigma_{xy}(0)\rangle\,\mathrm{d}t,$$

where k_B is the Boltzmann constant, T is temperature, V is the simulation cell volume and σ_{xy} is the xy component of the stress tensor. The average value of five independent off-diagonal components of the stress tensor (σ_{xy}, σ_{xz}, σ_{yz}, σ_{xx-yy} and $\sigma_{2zz-xx-yy}$), which is given by the plateau value of the running integral, is taken as the final viscosity. The calculated viscosities for ThF$_4$–LiF and ThF$_4$–LiF–BeF$_2$ are shown in Fig. 8. Relatively large viscosities in ThF$_4$–LiF–BeF$_2$ are observed compared with those in ThF$_4$–LiF, which may derive from the contribution of medium-range-ordered structural characters as detected above and strong electrostatic interaction between Be and F ions in ThF$_4$–LiF–BeF$_2$ molten salts, blocking the mobility of all ions. Importantly, with the increment of temperature, the viscosities plummet in the ThF$_4$–LiF–BeF$_2$ mixture. Given that electrostatic force is related to

Figure 8
The calculated viscosities for ThF$_4$–LiF and ThF$_4$–LiF–BeF$_2$ mixtures at several temperatures.

ion charge and the distance between two ions, no significant bond-distance elongation between Be and F ions was detected in previous structural analysis; therefore, electrostatic force is independent of temperature. However, the medium-range coordination shell in fluoride molten salts is affected considerably by temperature, as previously confirmed by XAFS analysis and MD simulations. This is a powerful illustration of the sensitivity of the medium-range-ordered networks to transport properties. In many previous reports (Dai *et al.*, 2015; Dewan *et al.*, 2013; Koslowski, 2000), the strong relationship between the structure and transport properties has also been researched. It is worth mentioning that EXAFS technique and *ab initio* MD simulations have proved powerful tools in resolving the short-to-medium-range order in highly disordered systems (Sheng *et al.*, 2006; Smith *et al.*, 2019; Witkowska *et al.*, 2005, 2006).

4. Conclusions

We conducted a systematic XAFS investigation of the thorium atom in ThF$_4$–LiF and ThF$_4$–LiF–BeF$_2$ eutectic salts in the solid state (room temperature) and molten states (600°C, 700°C and 800°C). Gradual pattern changes in the thorium L_3-edge XAFS data were observed, which contains a wealth of local geometric information. Three dominant complexes were found to coexist in the molten salts, $[ThF_7]^{3-}$, $[ThF_8]^{4-}$ and $[ThF_9]^{5-}$, with the eightfold-coordinated $[ThF_8]^{4-}$ molten salt always being the predominant one. Based on experimental and theoretical XAFS analysis, we revealed that the thorium and fluorine ions were exchanged more frequently in the ThF$_4$–LiF–BeF$_2$ molten salt and the local structure of thorium cations was much more disordered compared with that of the ThF$_4$–LiF molten salt. Importantly, the contribution of the medium-range-ordered coordination structure should not be ignored in fluorite molten salts. These local structural behaviors were further verified by MD simulations. We also eval-

uated the bonding strength in ThF$_4$–LiF and ThF$_4$–LiF–BeF$_2$ compounds. This work supports the contribution of the medium-range coordination shell in fluoride molten salts at high temperature, which has a significant impact on transport properties. Our work demonstrates the feasibility and unique potential of this method combining *in situ* XAFS spectroscopy and MD simulations to perform quantitative structure analysis of complex molten-salt systems at high temperatures.

References

Abram, T. & Ion, S. (2008). *Energy Policy*, **36**, 4323–4330.
Benfield, R. E., Filipponi, A., Bowron, D. T., Newport, R. J. & Gurman, S. J. (1994). *J. Phys. Condens. Matter*, **6**, 8429–8448.
Bessada, C., Rakhmatullin, A., Rollet, A.-L. & Zanghi, D. (2007). *J. Nucl. Mater.* **360**, 43–48.
Bunker, G. (1983). *Nucl. Instrum. Methods Phys. Res.* **207**, 437–444.
Dai, J., Long, D., Huai, P. & Li, Q. (2015). *J. Mol. Liq.* **211**, 747–753.
Delpech, S., Merle-Lucotte, E., Heuer, D., Allibert, M., Ghetta, V., Le-Brun, C., Doligez, X. & Picard, G. (2009). *J. Fluor. Chem.* **130**, 11–17.
Dewan, L. C., Simon, C., Madden, P. A., Hobbs, L. W. & Salanne, M. (2013). *J. Nucl. Mater.* **434**, 322–327.
Essmann, U., Perera, L., Berkowitz, M. L., Darden, T., Lee, H. & Pedersen, L. G. (1995). *J. Chem. Phys.* **103**, 8577–8593.
Ferlat, G., Cormier, L., Thibault, M. H., Galoisy, L., Calas, G., Delaye, J. M. & Ghaleb, D. (2006). *Phys. Rev. B*, **73**, 214207.
Ferlat, G., Soetens, J.-C., Miguel, A. S. & Bopp, P. A. (2005). *J. Phys. Condens. Matter*, **17**, S145–S157.
Filipponi, A. (2001). *J. Phys. Condens. Matter*, **13**, R23–R60.
Glover, W. J. & Madden, P. A. (2004). *J. Chem. Phys.* **121**, 7293–7303.
Gomilšek, J. P., Kodre, A., Arčon, I. & Hribar, M. (2003). *Phys. Rev. A*, **68**, 042505.
Guo, X., Qian, H., Dai, J., Liu, W., Hu, J., Shen, R. & Wang, J. (2019). *J. Mol. Liq.* **277**, 409–417.
He, S., Li, A., Yan, S., Li, X., Lin, J., Zou, Y. & Yu, X. (2012). Chinese Patent CN102590253A.
Hennig, C. (2007). *Phys. Rev. B*, **75**, 035120.
Hennig, C., Schmeide, K., Brendler, V., Moll, H., Tsushima, S. & Scheinost, A. C. (2007). *Inorg. Chem.* **46**, 5882–5892.
Hutter, J., Iannuzzi, M., Schiffmann, F. & VandeVondele, J. (2014). *WIREs Comput. Mol. Sci.* **4**, 15–25.
Ikeda-Ohno, A., Hennig, C., Rossberg, A., Funke, H., Scheinost, A. C., Bernhard, G. & Yaita, T. (2008). *Inorg. Chem.* **47**, 8294–8305.
Kelly, J. E. (2014). *Prog. Nucl. Energy*, **77**, 240–246.
Kodre, A., Arcon, I., Gomilsek, J. P., Preseren, R. & Frahm, R. (2002). *J. Phys. B At. Mol. Opt. Phys.* **35**, 3497–3513.
Koslowski, T. (2000). *J. Chem. Phys.* **113**, 10703–10711.

Laligant, Y., Le Bail, A., Avignant, D., Cousseins, J. C. & Ferey, G. (1989). *J. Solid State Chem.* **80**, 206–212.

Liu, J. B., Chen, X., Qiu, Y. H., Xu, C. F., Schwarz, W. H. & Li, J. (2014). *J. Phys. Chem. B*, **118**, 13954–13962.

Mathieu, L., Heuer, D., Brissot, R., Garzenne, C., Le Brun, C., Lecarpentier, D., Liatard, E., Loiseaux, J. M., Méplan, O., Merle-Lucotte, E., Nuttin, A., Walle, E. & Wilson, J. (2006). *Prog. Nucl. Energy*, **48**, 664–679.

Matsuura, H., Watanabe, S., Akatsuka, H., Okamoto, Y. & Adya, A. K. (2009). *J. Fluor. Chem.* **130**, 53–60.

Nosé, S. (1984). *J. Chem. Phys.* **81**, 511–519.

Numakura, M., Okamoto, Y., Yaita, T., Shiwaku, H., Akatsuka, H., Nezu, A., Tajima, K., Shimohara, Y., Bessada, C., Pauvert, O., Zanghi, D., Chamelot, P. & Matsuura, H. (2010). *J. Fluor. Chem.* **131**, 1039–1043.

Numakura, M., Sato, N., Bessada, C., Okamoto, Y., Akatsuka, H., Nezu, A., Shimohara, Y., Tajima, K., Kawano, H., Nakahagi, T. & Matsuura, H. (2011). *Prog. Nucl. Energy*, **53**, 994–998.

Olander, D., Konashi, K. & Yamawaki, M. (2012). *Comprehensive Nuclear Materials*, pp. 313–357, edited by R. J. M. Konings. Amsterdam, Oxford, Wareham: Elsevier.

Pauvert, O., Salanne, M., Zanghi, D., Simon, C., Reguer, S., Thiaudière, D., Okamoto, Y., Matsuura, H. & Bessada, C. (2011). *J. Phys. Chem. B*, **115**, 9160–9167.

Pauvert, O., Zanghi, D., Salanne, M., Simon, C., Rakhmatullin, A., Matsuura, H., Okamoto, Y., Vivet, F. & Bessada, C. (2010). *J. Phys. Chem. B*, **114**, 6472–6479.

Ravel, B. & Newville, M. (2005). *J. Synchrotron Rad.* **12**, 537–541.

Rehr, J. J., Kas, J. J., Vila, F. D., Prange, M. P. & Jorissen, K. (2010). *Phys. Chem. Chem. Phys.* **12**, 5503–5513.

Rollet, A.-L., Bessada, C., Auger, Y., Melin, P., Gailhanou, M. & Thiaudiere, D. (2004). *Nucl. Instrum. Methods Phys. Res. B*, **226**, 447–452.

Rollet, A.-L., Bessada, C., Rakhmatoulline, A., Auger, Y., Melin, P., Gailhanou, M. & Thiaudière, D. (2004). *C. R. Chim.* **7**, 1135–1140.

Rollet, A.-L., Rakhmatullin, A. & Bessada, C. (2005). *Int. J. Thermophys.* **26**, 1115–1125.

Salanne, M., Simon, C., Turq, P., Heaton, R. J. & Madden, P. A. (2006). *J. Phys. Chem. B*, **110**, 11461–11467.

Salanne, M., Simon, C., Turq, P. & Madden, P. A. (2007). *J. Phys. Chem. B*, **111**, 4678–4684.

Sandström, M., Persson, I., Jalilehvand, F., Lindquist-Reis, P., Spångberg, D. & Hermansson, K. (2001). *J. Synchrotron Rad.* **8**, 657–659.

Sheng, H. W., Luo, W. K., Alamgir, F. M., Bai, J. M. & Ma, E. (2006). *Nature*, **439**, 419–425.

Smith, A. L., Verleg, M. N., Vlieland, J., de Haas, D., Ocadiz-Flores, J. A., Martin, P., Rothe, J., Dardenne, K., Salanne, M., Gheribi, A. E., Capelli, E., van Eijck, L. & Konings, R. J. M. (2019). *J. Synchrotron Rad.* **26**, 124–136.

Toth, L. M. (1971). *J. Phys. Chem.* **75**, 631–636.

Toth, L. M. & Boyd, G. E. (1973). *J. Phys. Chem.* **77**, 2654–2657.

Toth, L. M., Quist, A. S. & Boyd, G. E. (1973). *J. Phys. Chem.* **77**, 1384–1388.

Wang, S., Luo, H., Deng, H., Xiao, S. & Hu, W. (2017). *J. Mol. Liq.* **234**, 220–226.

Watanabe, S., Adya, A. K., Okamoto, Y., Umesaki, N., Honma, T., Deguchi, H., Horiuchi, M., Yamamoto, T., Noguchi, S., Takase, K., Kajinami, A., Sakamoto, T., Hatcho, M., Kitamura, N., Akatsuka, H. & Matsuura, H. (2006). *J. Alloys Compd.* **408–412**, 71–75.

Watanabe, S., Matsuura, H., Akatsuka, H., Okamoto, Y. & Madden, P. A. (2005). *J. Nucl. Mater.* **344**, 104–108.

Witkowska, A., Rybicki, J. & Di Cicco, A. (2005). *J. Alloys Compd.* **401**, 135–144.

Witkowska, A., Rybicki, J., Panfilis, S. D. & Cicco, A. D. (2006). *J. Non-Cryst. Solids*, **352**, 4351–4355.

Xu, H. (2016). *Proceedings of the Thorium Energy Conference (ThEC13)*, 27–31 October 2013. CERN, Globe of Science and Innovation, Geneva, Switzerland. Cham: Springer.

Xu, H., Dai, Z. & Cai, X. (2014). *Nucl. Phys. News*, **24**, 24–30.

Yu, H., Wei, X., Li, J., Gu, S., Zhang, S., Wang, L., Ma, J., Li, L., Gao, Q., Si, R., Sun, F., Wang, Y., Song, F., Xu, H., Yu, X., Zou, Y., Wang, J., Jiang, Z. & Huang, Y. (2015). *Nucl. Sci. Tech.* **26**, 050102.

Zhang, L., Qie, M., Su, J., Zhang, S., Zhou, J., Li, J., Wang, Y., Yang, S., Wang, S., Li, J., Wu, G. & Wang, J.-Q. (2018). *J. Synchrotron Rad.* **25**, 514–522.

Zong, G., Cui, Z.-H., Sun, X.-G. & Xiao, J.-C. (2016). *J. Fluor. Chem.* **181**, 30–35.